Signal Separation in GEO SAR Imaging of Maneuvering Ships by Removing Micro-Motion Effect

Jindong Yu, *Student Member, IEEE*, Ze Yu, *Member, IEEE*, Yukun Guo, and Chunsheng Li

Abstract—**Geosynchronous synthetic aperture radar system provides the capability of continuous observation for several hours, which is of great significance for ship monitoring. The complex motion of maneuvering ship during long integration time makes the signals of different targets interfere with each other, resulting in the micro-motion effect, which degrades the quality of the image. The micro-motion of the expected target is first compensated for by the generalized radon-Fourier transform based method. The key of the algorithm is to enlarge the range cell migration of the interfering target while maintaining the energy of the expected target in a range bin based on the Keystone transform (KT) and inverse KT. Combined with the L-statistics method, the proposed algorithm can separate signals effectively. Validation results based on simulation and airborne experiments show that the proposed algorithm achieves good signal separation performance.**

Index Terms—**Geosynchronous synthetic aperture radar (GEO SAR), keystone transform, micro-motion removal.**

I. INTRODUCTION

FOR synthetic aperture radar (SAR), the range migration curve of each scatterer must be corrected precisely to accomplish coherent imaging with high quality. Maneuvering ships swing because of natural factors including waves and wind, as well as the stability systems of ships. Moreover, the swing amplitudes of different positions on the ship are different. As a result, the range migration curves corresponding to scatterers on the ship fluctuate and are entangled with each other, which causes signal aliasing. This effect becomes more serious as the aperture time increases, which affects the imaging quality of geosynchronous SAR (GEO SAR) whose aperture time is much longer than the swing period [1], [2]. This article focuses on signal separation, which is important to GEO imaging of maneuvering ships.

Swing of a ship can be modeled by micro-motion [3], [4]. The key to the aforementioned signal separation problem is to remove the micro-motion effect, which causes the leakage of energy from other scatterers in the signal of each scatterer. Some algorithms for micro-motion removal have been proposed. Inverse Radon transform [5] and Hough transform [6] are used to extract micro-motion features of signals with standard forms such as straight lines and sinusoids in the time-frequency (TF) plane, and then the micro-motion effect is filtered out. However, these methods may not be suitable for irregular micro-motion during long aperture time. Joint TF analysis and wavelet transform are applied to decompose signals and separate micro-motion signals from other signals. Then, the expected signal is reconstructed [7]. However, it is difficult for these methods to obtain high resolution in both the time and frequency domains [8]. Histogram analysis method assumes that the micro-motion signals appear less frequently in each frequency bin, and the signal with low frequency of occurrence in histogram is removed [8]. L-statistics method suppresses the micro-motion effect by removing the maximum energy in each frequency bin [9], which is more suitable for processing the nonconstant scattering of ships in long aperture time compared with other methods. However, both Histogram analysis method and L-statistics method cannot be used to maneuvering ships in GEO SAR because there is no static target in echo.

This article presents a three-step algorithm to remove the micro-motion effect in GEO SAR imaging of maneuvering ships. The key to the algorithm is to enlarge the range cell migration (RCM) of the interfering target while keeping the expected energy in a range bin based on the Keystone transform (KT) and inverse KT (IKT). Combined with the generalized radon-Fourier transform (GRFT) and L-statistics method, the proposed algorithm can separate signals effectively.

The rest of this article is organized as follows. Section II constructs a GEO SAR echo model for maneuvering ships and analyzes the micro-motion effect. Section III describes the basic idea of the micro-motion removal and signal separation. Then, the details of the proposed three-step algorithm are discussed in Section IV. Section V demonstrates the experiment results and validates the proposed method. Finally, Section VI concludes this article.

Manuscript received January 5, 2021; revised May 11, 2021, August 3, 2021, and October 16, 2021; accepted December 22, 2021. Date of publication December 29, 2021; date of current version January 12, 2022. *(Corresponding author: Ze Yu.)*

The authors are with the School of Electronics and Information Engineering, Beihang University, Beijing 100191, China (e-mail: yujindong92@163.com; yz613@buaa.edu.cn; venik123@buaa.edu.cn; 00178@buaa.edu.cn).

Digital Object Identifier 10.1109/JSTARS.2021.3139112

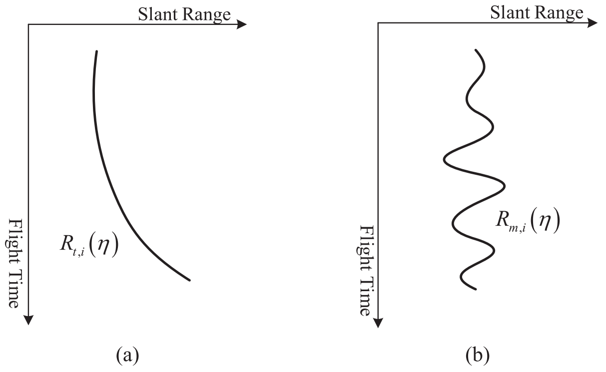

Fig. 1. Illustration of translation and micro-motion components. (a) and (b) represent the RCM of translation and micro-motion components, respectively.

II. Echo Model and Micro-Motion Effect

A ship can be modeled as the composition of several scatterers [10]. After range compression, the GEO SAR echo from the ith scatterer can be modeled as follows:

$$S_{rc}(\tau,\eta) = A_0 p_r\left[\tau - \frac{2R_i(\eta)}{c}\right] w_a(\eta-\eta_i) \exp\left[-j4\pi f_c \frac{R_i(\eta)}{c}\right]. \quad (1)$$

τ is the range fast time and η is the azimuth slow time, A_0 is a complex constant, η_i is the beam center crossing time, p_r is a sinc function in the range direction and $w_a(\eta)$ is the weighting window in the azimuthal direction, c denotes the velocity of light, f_c is the carrier frequency, and $R_i(\eta)$ depicts the slant range between the SAR and the ith scatterer.

A. Slant Range

The motion of a maneuvering ship is decomposed as the translation of an arbitrary reference point and the micro-motion of the body around that point [2], [3], [11]. Therefore, $R_i(\eta)$ in (1) can be decomposed into

$$R_i(\eta) = R_{t,i}(\eta) + R_{m,i}(\eta) \quad (2)$$

where $R_{t,i}(\eta)$ and $R_{m,i}(\eta)$ correspond to the projection of translation and micro-motion components in the SAR line-of-sight, respectively, as illustrated in Fig. 1.

Considering the long integration time of GEO SAR [12], [13] and the atmospheric turbulence [14]–[16], $R_{t,i}(\eta)$ is represented by an N_t-order polynomial as follows:

$$R_{t,i}(\eta) = R_0 + \sum_{n=1}^{N_t} r_n(\eta-\eta_i)^n. \quad (3)$$

R_0 denotes the slant range at η_i. Each coefficient $r_n$depends on ephemeris data, geographic information of the target zone [12], [13] and the atmospheric turbulence [14]–[16]. The detailed description is given in Appendix A.

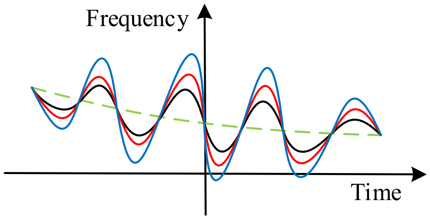

Fig. 2. Time-frequency curves with black, red, and blue colors corresponding to different scatterers on the same ship. They have the same translation represented by the dash line.

The micro-motion is the composition of sinusoidal functions [2], and $R_{m,i}(\eta)$ satisfies the following:

$$R_{m,i}(\eta) = \sum_{k=1}^{K} A_{k,i}\sin\left[\omega_{k,i}(\eta-\eta_i)+\theta_{k,i}\right] \quad (4)$$

where $A_{k,i}$, $\omega_{k,i}$, and $\theta_{k,i}$ represent the amplitude, angular frequency, and initial phase of the kth component, respectively.

B. Micro-Motion Effect

According to (2)–(4), the time-frequency relationship is as follows:

$$f_i = -\frac{2}{\lambda}\left\{\sum_{n=1}^{N_t} r_n n(\eta-\eta_i)^{n-1} + \sum_{k=1}^{K} A_{k,i}\omega_{k,i}\cos\left[\omega_{k,i}(\eta-\eta_i)+\theta_{k,i}\right]\right\}. \quad (5)$$

The last term in (5) represents the frequency modulation caused by micro-motion.

For the reference point, $A_{k,i}=0$. Therefore, the time-frequency curve does not fluctuate, as shown by the dashed line in Fig. 2. Other curves with different colors represent the time-frequency characteristics of three different scatterers on the same ship. Although they belong to the same ship and share the same angular frequency, i.e., $\omega_{k,i}=\omega_k$, the amplitudes and initial phases that are related to the distances from the reference point are different. The closer the scatterer is to the reference point, the smaller the amplitude of the curve.

Fig. 3(a) shows two adjacent scatterers P_A and P_B. Their time-frequency relationships are represented by blue and red curves in Fig. 3(b), respectively. Since the micro-motion parameters of scatterers are different, it is necessary to design a unique matched filter for each scatterer. By applying matched filtering, the micro-motion effect on P_A is totally removed and the blue curve becomes flat. However, due to mismatching, the signal of P_B is still modulated by the micro-motion and the red curve in Fig. 3(c) fluctuates. If Fourier transform is directly performed on P_A in the azimuth direction after micro-motion compensation, the imaging result of P_A will be degraded because of the interference caused by micro-motion of P_B, as shown in Fig. 3(d). Therefore, signal separation must be performed by removing the micro-motion effect to guarantee the imaging quality.

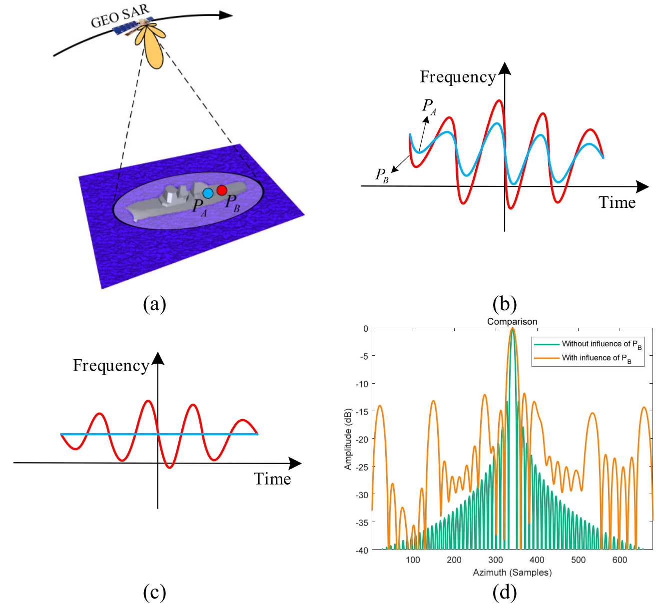

(a) (b) (c) (d)

Fig. 3. Illustration of micro-motion effect. (a) Observation geometry, where P_A and P_B belonging to the same ship are represented by blue and red scatterers, respectively. (b) Time-frequency relationship of P_A and P_B, depicted by blue and red curves, respectively. (c) Time-frequency relationship after compensation of the motion of P_A. (d) Imaging result in the azimuth direction. The green one is the imaging result of P_A without influence of P_B. The orange one is the imaging result of P_A with the influence of P_B, whose sidelobes and grating lobes increase and the resolution decreases as well.

III. Basic Idea of Signal Separation

Since the time-frequency characteristics of various scatterers are different, imaging needs to be performed scatterer by scatterer.

A three-step algorithm, which is composed of GRFT-based motion compensation, partial micro-motion removal and intersections removal, is proposed here, as illustrated in Fig. 4. The input of the algorithm is the range compression signal $S_{rc}(\tau,\eta)$.

In step 1, the signal with the strongest magnitude corresponds to the scatterer P_A (current strongest scatterer), whose RCM trajectory crosses range bins A–D, as shown by the blue curve in Fig. 4(a). Another scatterer is represented by the scatterer P_B, whose RCM trajectory crosses range bins A–E, as shown by the red curve in Fig. 4(a). GRFT is utilized to estimate the motion parameters of scatterer P_A by parameter searching. Then, a filter based on the estimation result is constructed to accomplish phase compensation and range cell migration correction (RCMC) of scatterer P_A. The result $S_{\mathrm{grft}}(\tau,\eta)$ in azimuth time and range time domain is shown in Fig. 4(b).

In step 2, KT [17] and IKT are used to enlarge the difference of energy distribution between scatterers in the range direction in azimuth-time and range time domain, and partially remove the micro-motion effect. By applying KT, the signal corresponding to scatterer P_B generates an azimuth time modulation, which enlarges the number of range bins that the RCM trajectory crosses, as the red curve in Fig. 4(c) shows. However, the degree of defocusing increases in the range direction at the same time. The trajectory of the RCM corresponding to scatterer P_A is maintained in range bin C during the integration time, as shown by the blue curve in Fig. 4(c). The result of KT is $S_{\mathrm{KT}}(\tau,t_a)$, where t_a is the azimuth time after scaling. A suitable window function filter in the range direction, such as the Hanning function, is applied to remove the energy except range bin C, i.e., only the energy in range bin C is retained. The result of range filtering $S_w(\tau,t_a)$ is shown in Fig. 4(d). Then, by applying IKT, the azimuth time modulation generated by KT is eliminated, which reduces the number of range bins crossed by scatterer P_B and recovers the focusing degree in the range direction. The result of IKT $S_{\mathrm{IKT}}(\tau,\eta)$ is shown in Fig. 4(e). The removed signal by range filter after IKT forms the complement set of Fig. 4(e), which is the input of GRFT when processing the next scatterer.

In step 3, the signal from range bin C is extracted and transformed to the time-frequency domain by short-time Fourier transform (STFT) [10]. The result $\mathrm{STFT}(\eta,f_\eta)$ is in azimuth time and azimuth frequency domain, and is shown in Fig. 4(f). Then, the L-statistics method is utilized to remove $(N-N\cdot Q)$ STFT entries with the highest magnitudes in each frequency bin, where N is the total number of the STFT entries and Q is the percentage of the retained STFT entries [9]. The result of intersections removal $\mathrm{STFT}_m(\eta,f_\eta)$ is shown in Fig. 4(g).

The output of this iteration is the extracted signal of the scatterer P_A (current strongest scatterer). It is worth noting that raw range compressed data shown in Fig. 4(a) are set as the input in each iteration. With the estimated parameters by GRFT, the next scatterer is processed in the same way as the scatterer P_A in Fig. 4.

IV. Three-Step Algorithm

The three-step algorithm is demonstrated in detail in this section.

A. GRFT-Based Phase Compensation

The GRFT of $S_{rc}(\tau,\eta)$ is expressed as follows [18], [19]:

$$S_{\mathrm{GRFT}} = \int S_{rc}\left[2\hat{R}(\eta)\big/c,\eta\right]\exp\left[j\frac{4\pi}{\lambda}\hat{R}(\eta)\right]d\eta \tag{6}$$

where

$$\hat{R}(\eta)=\sum_{n=0}^{N_t}\hat{r}_n\eta^n+\sum_{k=1}^{K}\hat{A}_{k,m}\sin\left(\hat{\omega}_{k,m}\eta+\hat{\theta}_{k,m}\right). \tag{7}$$

The subscript "m" in (7) refers to the strongest scatterer of the ship. $\hat{r}_n$, $\hat{A}_{k,m}$, $\hat{\omega}_{k,m}$, and $\hat{\theta}_{k,m}$ represent the motion parameters of the strongest scatterer, i.e., the expected scatterer to be extracted, and are estimated according to the following:

$$\left[\hat{r}_n,\hat{A}_{k,m},\hat{\omega}_{k,m},\hat{\theta}_{k,m}\right]=\underset{\left(\hat{r}_n,\hat{A}_{k,m},\hat{\omega}_{k,m},\hat{\theta}_{k,m}\right)}{\arg\max}\left|S_{\mathrm{GRFT}}\right|. \tag{8}$$

Based on the estimated result, RCMC and phase compensation can be accomplished for the scatterer P_A. By transforming (1) into the range-frequency domain, the signal is expressed as

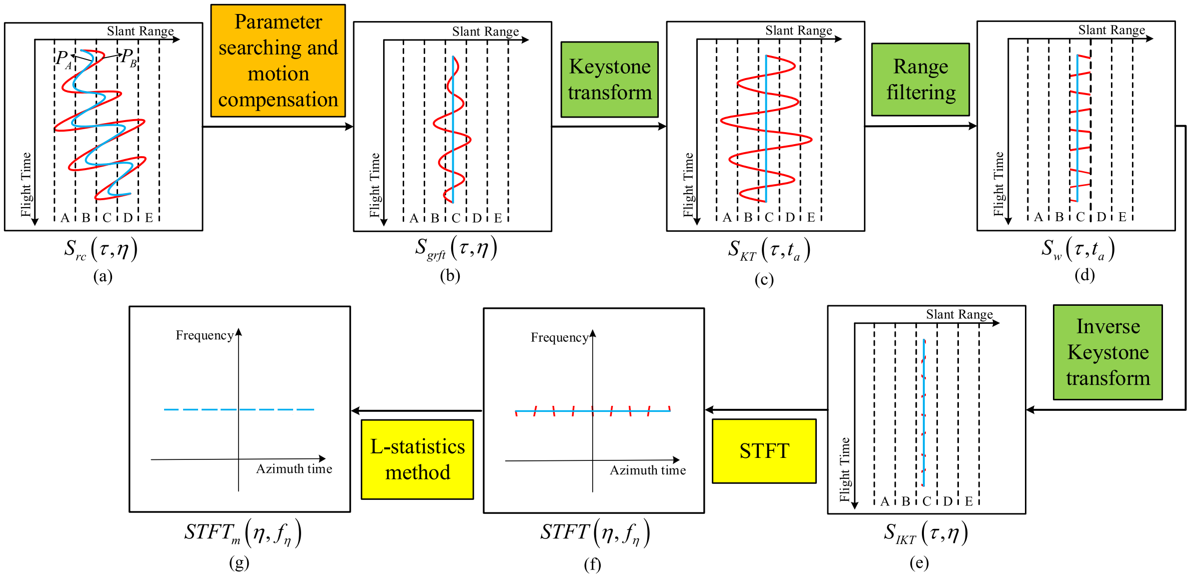

$S_{rc}(\tau,\eta)$ (a) $S_{grft}(\tau,\eta)$ (b) $S_{KT}(\tau,t_a)$ (c) $S_{w}(\tau,t_a)$ (d) $STFT_m(\eta,f_\eta)$ (g) $STFT(\eta,f_\eta)$ (f) $S_{IKT}(\tau,\eta)$ (e)

Fig. 4. Illustration of the proposed algorithm, where the operations in the orange, green, and yellow box belongs to steps 1, 2, and 3, respectively. The symbols of the signals are shown in (a)–(g). The dashed lines with capital letters in (a)–(e) represent the range bins. (a) RCM of the range compression signal, where P_A and P_B are represented by blue and red curves, respectively. (b) Result after motion compensation of P_A by GRFT-based method. (c) KT result of (b). (d) Range filtering result of (c). (e) IKT result of (d). (f) Time-frequency relationship of range bin C by STFT. (g) L-statistics method result of (g).

follows:

$$S_{rc}\left(f_\tau,\eta\right)=U\left(f_\tau,\eta\right)\exp\left[-j\frac{4\pi}{c}\left(f_c+f_\tau\right)R_i\left(\eta\right)\right] \tag{9}$$

where

$$U\left(f_\tau,\eta\right)=\mathcal{F}_\tau\left[A_0p_r\left(\tau\right)w_a\left(\eta-\eta_i\right)\right]. \tag{10}$$

By applying the following filter:

$$H_{grft}\left(f_\tau,\eta\right)=\exp\left[j\frac{4\pi}{c}\left(f_c+f_\tau\right)\cdot\hat{R}\left(\eta\right)\right] \tag{11}$$

and inverse Fourier transform in the range direction, the signal becomes (see Appendix B)

$$\begin{aligned}S_{\mathrm{grft}}\left(\tau,\eta\right)&=\mathcal{F}_\tau^{-1}\left[S_{rc}\left(f_\tau,\eta\right)\times H_{\mathrm{grft}}\left(f_\tau,\eta\right)\right]\\&=A_0p_r\left[\tau-\frac{2R_{\mathrm{grft}}\left(\eta\right)}{c}\right]w_a\left(\eta-\eta_i\right)\\&\quad\times\exp\left[-j4\pi f_c\frac{R_{\mathrm{grft}}\left(\eta\right)}{c}\right]\end{aligned} \tag{12}$$

where

$$R_{\mathrm{grft}}\left(\eta\right)=R_0'+{r_1}'\eta+\sum_{k=1}^{K'}{A'}_{k,i}\sin\left({\omega'}_{k,i}\eta+{\theta'}_{k,i}\right)$$

$$R_0'=R_0-r_1\eta_i+r_2{\eta_i}^2$$

and

$${r_1}'=r_1-2r_2\eta_i-\hat{r}_1.$$

${A'}_{k,i}$, ${\omega'}_{k,i}$, and ${\theta'}_{k,i}$ satisfy

$$\begin{aligned}&\sum_{k=1}^{K'}{A'}_{k,i}\sin\left({\omega'}_{k,i}\eta+{\theta'}_{k,i}\right)\\&=\sum_{k=1}^{K}A_{k,i}\sin\left[\omega_{k,i}\left(\eta-\eta_i\right)+\theta_{k,i}\right]\\&\quad-\sum_{k=1}^{K}\hat{A}_{k,m}\sin\left(\hat{\omega}_{k,m}\eta+\hat{\theta}_{k,m}\right).\end{aligned} \tag{13}$$

Fig. 4(a) and (b) show the RCM of the two scatterers before and after compensation by filtering. The time-frequency relationship of the two scatterers before and after compensation can be seen in Fig. 3(b) and (c).

After GRFT-based motion compensation, for scatterer P_A, ${r_1}'$ and $A'_{k,i}$ are equal to zero. Thus, the residual slant range is R_0', as shown by the blue curve in Fig. 4(b), which indicates that the energy of scatterer P_A is maintained in a range bin during the integration time.

However, for other scatterers, such as the adjacent scatterer P_B, the residual slant range is affected by ${r_1}'$, $A'_{k,i}$, $\omega'_{k,i}$, and $\theta'_{k,i}$. When the difference in slant ranges between the two adjacent scatterers is less than a range bin, their energy is aliased in the same range bin.

B. Partial Micro-Motion Removal Based on KT and IKT

By applying KT to (12) [17], the following expression can be achieved (see Appendix C):

$$S_{\mathrm{KT}}\left(f_\tau,t_a\right)={w_a}'\left(t_a\right)\mathcal{F}_\tau\left[p_r\left(\tau\right)\right]\exp\left[j\varphi\left(f_\tau,t_a\right)\right] \tag{14}$$

where

$$\varphi\left(f_\tau, t_a\right) = -\frac{4\pi}{\lambda}\left[{R_0}' + {r_1}' t_a + \sum_{k=1}^{K'} {A'}_{k,i} \sin\left({\omega'}_{k,i} t_a + {\theta'}_{k,i}\right)\right] - \frac{4\pi}{c}\left[D_1 f_\tau + D_2 {f_\tau}^2 + D_3 {f_\tau}^3 + \Delta\left(f_\tau\right)\right] \tag{15}$$

and t_a is the azimuth time after scaling, i.e.

$$t_a = \frac{f_c + f_\tau}{f_c}\eta. \tag{16}$$

KT is a scaling operation, which transforms η to a new azimuth time t_a according to (16). After inverse Fourier transform in the range direction, (14) becomes as follows:

$$S_{\mathrm{KT}}\left(\tau, t_a\right) = {w_a}'\left(t_a\right) w_r\left(\tau, t_a\right) \times \exp\left\{-j\frac{4\pi}{\lambda}\left[{R_0}' + {r_1}' t_a + \sum_{k=1}^{K'} {A'}_{k,i} \sin\left({\omega'}_{k,i} t_a + {\theta'}_{k,i}\right)\right]\right\} \tag{17}$$

where

$$w_r\left(\tau, t_a\right) = {\mathcal{F}_\tau}^{-1}\left[\exp\left\{-j\frac{4\pi}{c}\begin{bmatrix} R_{KT}\left(t_a\right) f_\tau \\ +D_2 {f_\tau}^2 + D_3 {f_\tau}^3 + \Delta\left(f_\tau\right)\end{bmatrix}\right\}\right]. \tag{18}$$

For scatterer P_A, $A'_{k,i}$, D_2, D_3, and $\Delta(f_\tau)$ are all equal to 0. $R_{KT}(t_a)$ can be simplified as R'_0 and (18) is written as follows:

$$w_{r\_A}\left(\tau, t_a\right) = \mathrm{sinc}\left[\mathrm{Br}\left(\tau - \frac{2{R_0}'}{c}\right)\right]. \tag{19}$$

The energy of the scatterer P_A is concentrated in the range bin whose slant range is R'_0.

For scatterer P_B, (18) is written as follows:

$$w_{r\_B}\left(\tau, t_a\right) = \mathrm{sinc}\left[\mathrm{Br}\left(\tau - \frac{2R_{KT}\left(t_a\right)}{c}\right)\right] \otimes {\mathcal{F}_\tau}^{-1}\left[\exp\left\{-j\frac{4\pi}{c}\left[D_2 {f_\tau}^2 + D_3 {f_\tau}^3 + \Delta\left(f_\tau\right)\right]\right\}\right] \tag{20}$$

where $\otimes$ represents the convolution operation, and $R_{KT}(t_a)$ is expressed as follows:

$$R_{\mathrm{KT}}\left(t_a\right) = R'_0 + \sum_{k=1}^{K'}\begin{bmatrix} {A'}_{k,i} \sin\left({\omega'}_{k,i} t_a + {\theta'}_{k,i}\right) \\ -{A'}_{k,i}{\omega'}_{k,i} t_a \cos\left({\omega'}_{k,i} t_a + {\theta'}_{k,i}\right)\end{bmatrix}. \tag{21}$$

Compared with the trajectory of RCM $R_{\mathrm{grft}}(\eta)$ in Fig. 4(b) before KT, $R_{\mathrm{KT}}(t_a)$ eliminates the first-order term ${r_1}'\eta$ and generates new sine terms modulated by t_a, i.e., $\sum_k -{A'}_{k,i}{\omega'}_{k,i}t_a\cos({\omega'}_{k,i}t_a + {\theta'}_{k,i})$. These terms enlarge the RCM of scatterer P_B in the range direction by a multiple of azimuth time and spread in more range bins, as shown in Fig. 4(c). Compared with Fig. 4(b), the distance between scatterers P_A and P_B is enlarged in Fig. 4(c). The spread energy of scatterer P_B is separated from aliasing with scatterer P_A in range bin C, which is then removed by a filter designed as follows:

$$H_w\left(\tau\right) = \mathrm{rect}\left[\frac{\tau - 2{R_0}'/c}{T_r}\right] \tag{22}$$

where $\mathrm{rect}[\cdot]$ is a window function in the form of a rectangle and T_r is the time duration of a range bin. Filtering result $S_w(\tau, t_a)$ can be expressed as follows:

$$S_w\left(\tau, t_a\right) = {w_a}'\left(t_a\right) {w_r}'\left(\tau, t_a\right) \times \exp\left\{-j\frac{4\pi}{\lambda}\left[{R_0}' + {r_1}' t_a + \sum_{k=1}^{K'} {A'}_{k,i} \sin\left({\omega'}_{k,i} t_a + {\theta'}_{k,i}\right)\right]\right\} \tag{23}$$

where ${w_r}'(\tau, t_a) = w_r(\tau, t_a) \cdot H_w(\tau)$ can be seen as a window function with interceptive RCM located in a range bin as depicted in Fig. 4(d).

However, the high-order terms, i.e., $D_2{f_\tau}^2$, $D_3{f_\tau}^3$, and $\Delta(f_\tau)$ in (20), defocus $w_{r\_B}(\tau, t_a)$ in the range direction, as shown in Fig. 4(d). Equation (59) indicates that D_2, D_3 and the coefficients of the high-order terms in $\Delta(f_\tau)$ become larger with increasing t_a, which increases the degree of defocusing in the range direction. This range defocusing makes partial energy of scatterer P_B which has no intersection with scatterer P_A before KT aliased with scatterer P_A. Therefore, the scope of intersections in the azimuth direction of scatterers P_A and P_B enlarges after KT, which is shown in Fig. 4(d).

In order to solve the defocusing problems caused by KT, IKT is developed here, which makes an inverse scaling between the azimuth time and range frequency, i.e.

$$t_a = \frac{f_c + f_\tau}{f_c}\eta \tag{24}$$

where t_a and η represent the azimuth time before and after IKT, respectively.

By applying IKT to (23), the result is as follows (see Appendix D):

$$S_{\mathrm{IKT}}\left(\tau, \eta\right) = {w_a}'\left(\eta\right) w_{s,i}\left(\tau, \eta\right) p_r\left[\tau - \frac{2R_{\mathrm{IKT}}\left(\eta\right)}{c}\right] \times \exp\left\{-j\frac{4\pi}{\lambda}R_{\mathrm{IKT}}\left(\eta\right)\right\} \tag{25}$$

where $R_{\mathrm{IKT}}(\eta)$ has the same form with $R_{\mathrm{grft}}(\eta)$

$$R_{\mathrm{IKT}}\left(\eta\right) = R'_0 + {r_1}'\eta + \sum_{k=1}^{K'} {A'}_{k,i} \sin\left({\omega'}_{k,i}\eta + {\theta'}_{k,i}\right). \tag{26}$$

By applying the STFT to the signal located in the R'_0 range bin of (25), the signal in the time-frequency domain is as follows:

$$\mathrm{STFT}\left(n, m\right) = \sum_{i=0}^{N-1} S_{\mathrm{IKT}}\left({\tau'}_0, i\right) w\left(i - n\right) \exp\left(-j\frac{2\pi m i}{N}\right) \tag{27}$$

where

$$w\left(i\right) = \mathrm{rect}\left[\frac{i}{N_i}\right] \tag{28}$$

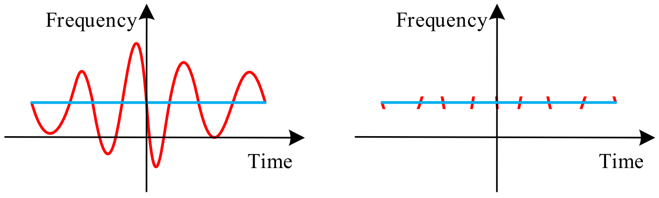

(a) (b)

Fig. 5. Time-frequency result before and after KT and IKT. (a) Time-frequency relationship before KT and IKT. (b) Time-frequency relationship after KT and IKT.

$\tau_0' = 2R'_0/c$. $S_{\text{IKT}}(\tau'_0, i)$ represents the discrete time signal from the R_0' range bin, n and m are the index of time and frequency, respectively, $N$is the length of $S_{\text{IKT}}(\tau'_0, i)$, and N_i is the number of discrete time series of a short time Fourier transform.

Equation (27) is illustrated in Fig. 5(a). The blue line represents the energy of the expected scatterer, while the red lines represent that of another scatterer with residual micro-motion. It is demonstrated that the micro-motion effect is partially removed and only intersections need to be further processed.

C. Intersections Removal

After the operation in part B, the interference from a scatterer with residual micro-motion exists at limited time samplings, which is denoted by the multisegment red curves in Fig. 5(b).

The spectrogram at each frequency bin can be sorted in an ascending order of $|\text{STFT}(n,m)|^2$ to form a new sequence $\text{STFT}_m(k,m), k \in [0, N-1]$. By setting a suitable percent Q, the largest $(N - NQ)$ elements of $\text{STFT}_m(k,m)$ are set to zero. Then, the final imaging result can be achieved as follows:

$$S_{\text{image}}(\tau_0', m) = \sum_{k=0}^{N\cdot Q-1} \text{STFT}_m(k,m). \tag{29}$$

It is demonstrated in [9] that the Fourier transform result can be reconstructed by summing all STFT complex values, which indicates that the energy of scatterer P_B can be removed in time-frequency domain and scatterer P_A remains. The TF curve of scatterer P_A is distributed in all time samplings but one frequency bin, as shown by the blue curve in Fig. 5. However, the TF curve of scatterer P_B is distributed in multiple frequency bins, as shown by the red curve in Fig. 5. Based on this difference in the distribution of scatterer P_A and scatterer P_B, L-statistics method is introduced, and the result can be seen from Fig. 4(g).

V. EXPERIMENTAL RESULTS AND ANALYSIS

The simulated data and real data are used to validate the proposed method. The simulation experiments are implemented based on the system parameters of GEO SAR in Table I [20], and the micro-motion parameters of a ship are listed in Table II. The simulated data can reflect the high-order slant range and the micro-motion of the target to a certain degree. Furthermore, real data are used to verify the effectiveness of the proposed algorithm, where the motion of ships is more complex.

TABLE I
SIMULATION PARAMETERS

Parameter	Value
Semi-major axis (km)	42164
Inclination (°)	10
Eccentricity	0
Longitude of ascend node (°)	100
Wavelength (m)	0.05
Integration time (s)	250
Pulse repetition frequency (Hz)	200
Longitude of scene center (°)	2
Latitude of scene center (°)	120

TABLE II
MOTION PARAMETERS OF SHIP

Parameter	Value
Position of ship barycenter (azimuth, range) (m)	(0,0)
Length of ship (m)	60
Width of ship (m)	10
Yaw period (s)	33
Yaw amplitude (°)	1.38
Pitch period (s)	11.2
Pitch amplitude (°)	0.9
Roll period (s)	26.4
Roll amplitude (°)	5
RCS of ship	7943.3

TABLE III
MAGNITUDES OF T_1–T_6

Target	T_1	T_2	T_3	T_4	T_5	T_6
Amplitude	14.86	29.10	9.56	10.20	11.24	29.09

The L-statistics method can remove micro-motion with a lower computational cost, and it does not need any prior knowledge of the motion of the target, which is suitable for situations of irregular micro-motion and time-frequency intersections compared with the existing methods. However, the L-statistics method in [9] is utilized to deal with static targets and targets with micro-motion, which means that this method cannot be used directly in this experiment where the targets all contain micro-motion. For better comparison, the micro-motion of scatterer P_A is compensated for first by GRFT-based method. Then, the L-statistics method is used to compare with the proposed method. Moreover, in order to verify the effectiveness of KT and IKT operation in micro-motion removal of scatterer P_B and energy preservation of scatterer P_A, traditional Fourier transform is introduced to compare with KT and IKT operation.

A. Simulated Data

As illustrated in Fig. 6, six isolated scatterers denoted by T_1–T_6 are deployed in a simulated scene. The interval between adjacent scatterers is 10 m, whose amplitudes are set in Table III. The parameters of the ship including size, motion period, and

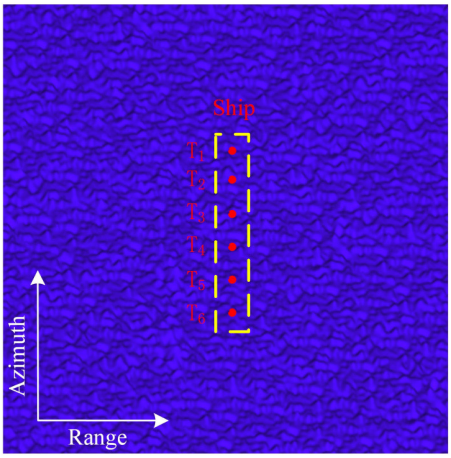

Fig. 6. Illustration of the simulated scene.

TABLE IV
EVALUATION OF IMAGING RESULTS OF THE SIMULATED DATA

		Azimuth Direction			Range Direction		
Method	Scatter	Res (m)	PSLR (dB)	ISLR (dB)	Res (m)	PSLR (dB)	ISLR (dB)
FT	T_1	4.70	-10.77	-6.68	5.08	-13.64	-9.63
	T_2	4.70	-12.23	-9.33	5.08	-12.96	-9.96
	T_3	4.70	-9.59	-2.77	5.08	-13.70	-8.75
KT and IKT	T_1	4.70	-11.15	-9.25	5.08	-13.74	-9.52
	T_2	4.70	-12.20	-9.86	5.08	-13.10	-10.12
	T_3	4.70	-10.10	-8.03	5.08	-14.01	-8.78
L statistics method	T_1	4.70	-11.30	-7.18	5.08	-13.76	-10.65
	T_2	4.70	-12.45	-9.20	5.08	-13.34	-10.66
	T_3	4.70	-10.04	-5.45	5.08	-13.75	-8.76
Proposed method	T_1	4.70	-12.98	-9.33	5.08	-13.88	-9.78
	T_2	4.70	-12.67	-10.17	5.08	-13.17	-10.38
	T_3	4.70	-10.34	-9.21	5.08	-14.14	-9.02

TABLE V
EXPERIMENTAL PARAMETERS OF REAL DATA

Parameter	**Value**
Velocity of platform (m/s)	5
Radar center frequency (GHz)	5.4
Integration time (s)	18
Pulse repetition frequency (Hz)	1000

TABLE VI
EVALUATION OF IMAGING RESULTS OF REAL DATA

		Azimuth Direction			Range Direction		
Method	Scatter	Res (m)	PSLR (dB)	ISLR (dB)	Res (m)	PSLR (dB)	ISLR (dB)
FT	S_1	0.75	-5.57	-3.70	1.00	-15.64	-10.96
	S_2	0.80	-7.81	-1.36	0.95	-11.56	-8.72
KT and IKT	S_1	0.80	-6.99	-4.58	1.05	-16.67	-10.86
	S_2	0.85	-8.89	-6.33	0.95	-11.75	-8.69
L-statistics method	S_1	0.75	-7.62	-5.69	1.00	-16.14	-12.31
	S_2	0.85	-10.08	-3.65	0.95	-10.76	-9.78
Proposed method	S_1	0.75	-10.09	-5.78	1.05	-17.51	-13.23
	S_2	0.80	-10.11	-7.40	0.95	-11.75	-9.04

TABLE VII
PARAMETER ESTIMATION RESULTS OF TRANSLATION

Parameter Name	Truth Value	Estimated Value
$\hat{r}_0$	36402260	36402262
$\hat{r}_1$	0.0021	0.0018
$\hat{r}_2$	5.5165e-04	5.4747e-04

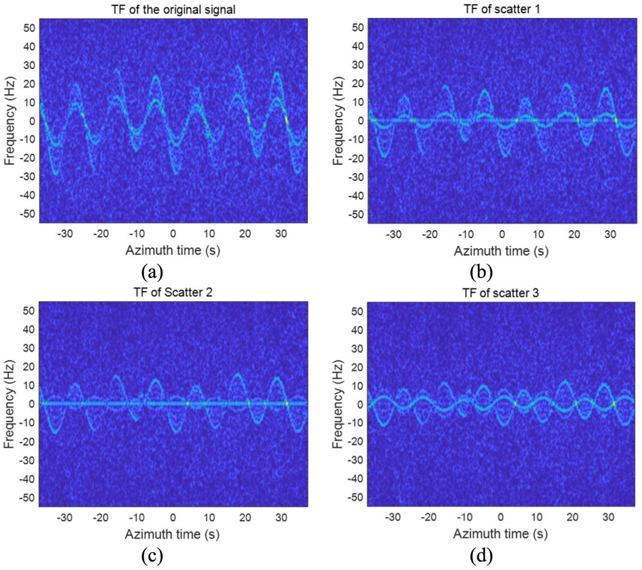

Fig. 7. Time-frequency results before and after GRFT. (a) is the TF relationship of the original signal. (b)–(d) represent the TF relationship of scatterers T_1, T_2, and T_3, respectively.

amplitude are listed in Table II under sea state five. Other simulation parameters, including orbital parameters and the position of the scene, are listed in Table I.

Scatterers T1, T2, and T3 represent the scatterer in a ship with medium amplitude, largest amplitude, and smallest amplitude, respectively. The GRFT estimation results of scatterers T1, T2, and T3 in a subaperture are listed in Tables VII–X in Appendix E. After motion compensation, the corresponding time-frequency relationships of scatterers T_1, T_2, and T_3 are shown in Fig. 7.

In order to demonstrate the separation effect of KT and IKT process, the range compressed results and the TF transform results of the scatterer, such as T_1, are shown in Fig. 8, where the results after motion compensation, KT, IKT, and the L-statistics method are shown in the first to fourth columns, respectively. Fig. 8(a) shows the range compressed and motion compensation result. Because there is clutter in the simulation data, the trajectory of the RCM cannot be seen in Fig. 8(a). In order to show the trajectory of RCM, sea clutter is removed from the simulation data temporarily and the range compressed result is shown in Fig. 8(b). But in practice, we still process the simulation data with clutter. The range compressed results of the data with clutter are shown in the first row, and the range compressed results of the data without clutter are shown in the second row. The TF transform results of the first row are shown in the third row.

From Fig. 8(b), it is known that multiple scatterers are aliased together in the range direction, and their RCM trajectories are mainly distributed in two range bins. Furthermore, the TF transform results of the two range bins with scatterers shown in

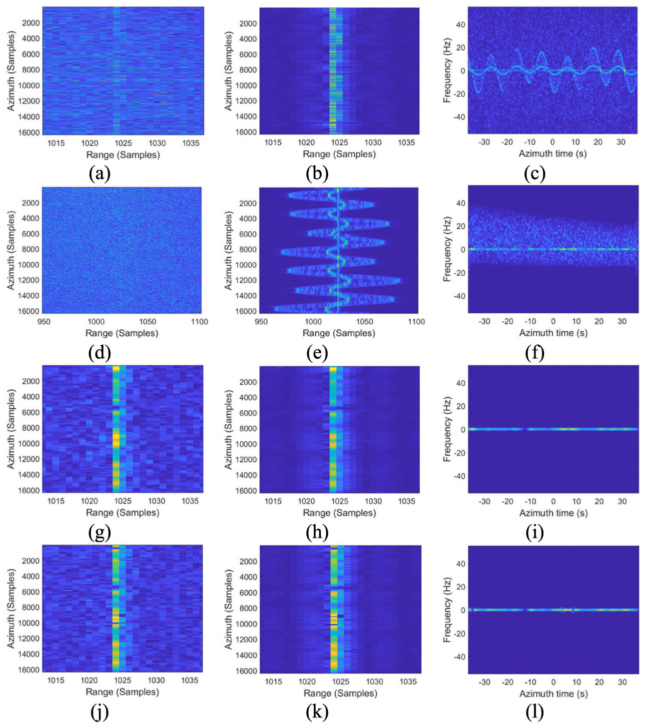

(a) (b) (c)
(d) (e) (f)
(g) (h) (i)
(j) (k) (l)

Fig. 8. Range compressed results and time-frequency transform results. (a), (d), (g), and (j) are the range compressed results after motion compensation, KT, IKT, and the L-statistics method, respectively. (b), (e), (h), and (k) represent the range compressed results of the data without clutter after motion compensation, KT, IKT, and the L-statistics method, respectively. (c), (f), (i), and (l) are the time-frequency transform results of (a), (d), (g), and (j), respectively.

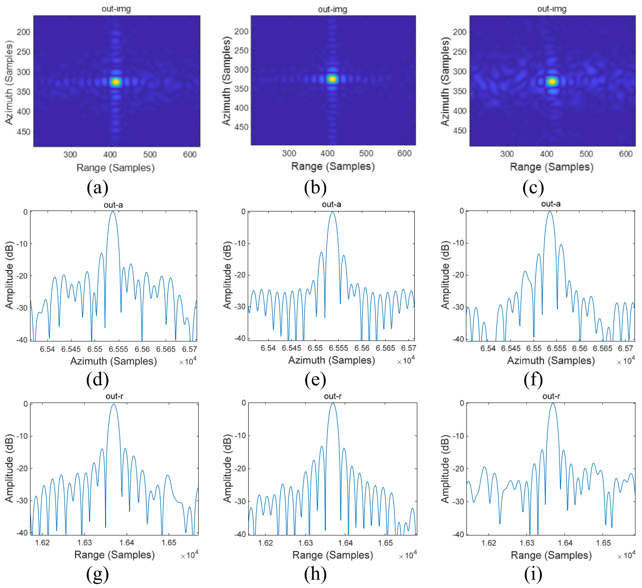

(a) (b) (c)
(d) (e) (f)
(g) (h) (i)

Fig. 9. Imaging results achieved by the proposed method. (a)–(c) Images of T_1, T_2, and T_3, respectively. (d)–(f) Azimuth profile of the three scatterers. (g)–(i) Range profile of the three scatterers.

Fig. 8(c) demonstrates that the scatterers have several intersections and interfere with each other in TF domain as well. Fig. 8(e) shows the range compressed results after KT. Compared with the results in Fig. 8(b) where all the scatterers are aliased in two range bins, KT makes the RCM of the desired scatterer keep within a range bin and that of other scatterers extend to more range bins. Then the energy of the scatterers extended to other range bins is removed by a filter. Fig. 8(h) and (i) show the range compressed result and TF transform result after IKT, respectively. Compared with the results in Fig. 8(b) and (c), the energy of other scatterers has been removed basically. Therefore, the KT and IKT process can well separate the signals of each scatterer. However, the energy of other scatterers still exists in the intersections between different TF curves in TF domain. In order to obtain a better micro-motion effect removal performance, the L-statistics method is introduced. The range compressed results and TF transform result after L-statistics method are shown in Fig. 8(j)—(l). It shows that the energy in the intersections is partly removed.

Fig. 9 illustrates the imaging results of the proposed method. The first, second, and third rows represent the results of T_1, T_2, and T_3, respectively. Images, azimuth profiles, and range profiles are illustrated in the first, second, and third columns, respectively. The imaging results achieved by the Fourier transform (FT), KT, and IKT, the L-statistics method, and the proposed method are evaluated by the resolution (Res), peak-to-side lobe ratio (PSLR), and integrated side lobe ratio (ISLR) in the azimuth and range directions, which are listed in Table IV. Since the FT and L-statistics method cannot be applied directly to this problem, the input of these two methods is the signal after GRFT compensation.

The FT method applies Fourier transform to the input signal in the azimuth direction for imaging, which does not contain a micro-motion removal operation. Thus, the result of the FT method can be seen as the reference. It is demonstrated that the imaging results of FT are greatly influenced by the signal amplitude. The ISLR of T_3 in the azimuth direction is only –2.77 dB, while the azimuth ISLR of T_2 corresponds to the strongest scatterer among T_1–T_6 is –9.33 dB. The L-statistics method separates signals by removing the micro-motion effect in the TF domain and achieves better imaging results. However, the higher ISLR of T_2 in the azimuth direction compared with the FT indicates that the useful data of T_2 are removed together with the micro-motion effect, leading to a high sidelobe level. The proposed KT and IKT operation removes partial energy of the micro-motion effect by enlarging the scope of RCM. Azimuth results of T_1–T_3 demonstrate the effectiveness of this operation in improving ISLR compared with the FT and L-statistics method. However, the PSLR in the azimuth direction is usually worse than that of the L-statistics method, which is caused by residual TF intersections.

The proposed method utilizes KT and IKT operations to reduce the percentage of energy removed in TF domain, which means that the method removes more energy from the micro-motion effect and reserves the useful data simultaneously. Compared with the above three methods, the proposed method achieves better imaging quality except for three indicators. The first indicator is the range ISLR of T_1, where the L-statistics method improves ISLR by 0.86 dB in the range direction at the expense of 2.15 dB ISLR degradation and 1.68 dB PSLR

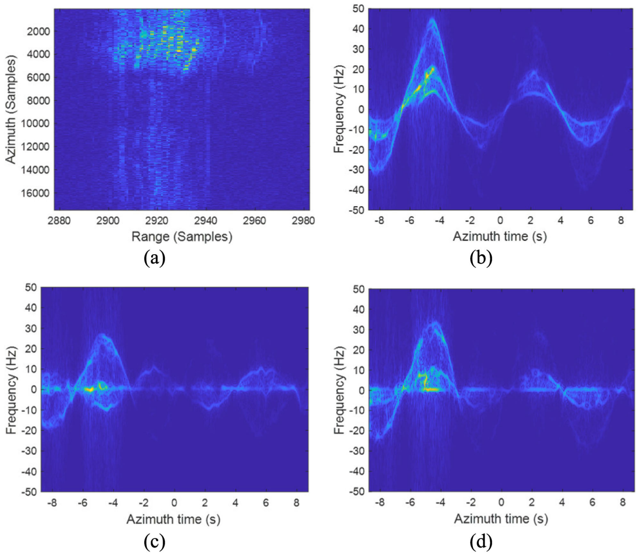

(a) (b)

(c) (d)

Fig. 10. Illustration of real data. (a) and (b) are range compressed result and TF representation of original data. (c) and (d) represent TF representations after GRFT of S_1 and S_2, respectively.

degradation in the azimuth direction. The second and third indicators are the PSLR and ISLR of T_2 in the range direction, where the L-statistics method improves ISLR by 0.28 dB in the range direction at the expense of 0.97 dB ISLR degradation in the azimuth direction. Therefore, taking both the azimuth and range directions into consideration, the proposed method achieves better signal separation performance.

B. Real Data

The real data are obtained by a helicopter platform with a velocity of 5 m/s. The parameters, including the PRF and the center frequency are listed in Table V. The airborne SAR observes a ship on the sea during the flight. Because of the low flight velocity, the synthetic aperture time is approximately 18 s and contains multiple micro-motion periods, which can more fully verify the proposed algorithm.

The result after range compression is shown in Fig. 10(a). The data from range bin 2906 to 2908 are selected and transformed into the time-frequency domain, as shown in Fig. 10(b), which contains multiple time-frequency intersections, and the magnitude of the TF curve is time-varying. The GRFT estimation results of the two scatterers in the data, denoted by S_1 and S_2, are listed in Tables XI and XII in Appendix D. After GRFT-based motion compensation, the time-frequency results of the two scatterers are illustrated in Fig. 10(c) and (d), respectively. When processing S_1, the motion of S_1 is compensated for. The residual micro-motion of other scatterers still exists and increases the sidelobes of S_1 after imaging. And this situation is same when processing S_2.

Fig. 11 shows the imaging results of S_1 and S_2 achieved by FT, KT, and IKT, the L-statistics method, and the proposed method, respectively. Images, azimuth profiles of S_1, range profiles of S_1, azimuth profiles of S_2, and range profiles of S_2 are illustrated in the first to fifth columns, respectively. The first to fourth rows represent the results achieved by FT, KT and IKT, the L-statistics method, and the proposed method, respectively. Imaging results are evaluated by resolution, PSLR, and ISLR in the azimuth and range directions, which are listed in Table VI. From the evaluation results, it is found that the proposed method achieves better imaging quality except for the ISLR of S_2 in the range direction. The L-statistics method improves ISLR by 0.738 dB in the range direction at the expense of 0.991 dB of PSLR degradation in the range direction and 3.752 dB of ISLR degradation in the azimuth direction. Therefore, taking both the azimuth and range directions into consideration, the proposed method achieves better signal separation performance.

C. Performance Analysis

SNR mainly depends on Noise equivalent sigma zero (NESZ), which is defined as the receiving energy that are equal to the backscattering coefficient of the thermal noise energy [21]. The NESZ of GEO SAR is designed to be –20 dB as described in [21] and [22]. The radar parameter design for GEO SAR including the transmitter power design and SNR analysis are demonstrated in [22] and [23], which verify that the SNR in GEO SAR is not a thorny problem. In addition, several GEO SAR static target imaging algorithms [24], [25], GEO SAR moving target imaging algorithm [19], GEO SAR rotating target imaging algorithm [2], and the GEO SAR equivalent experiment [26] also demonstrate that the SNR does not prevent GEO SAR imaging.

The performance of the proposed algorithm is mainly influenced by SCR, the position of scatterers and the relative motion between scatterers. SCR determines the parameter estimation accuracy. The positions of scatterers and the relative motion between them, such as the rotation motion, determinate the slant range history. Therefore, the separation problem is analyzed in two parts as follows.

The experiments in different clutter level are implemented in order to analyze the influence of clutter on estimation accuracy. And the results are shown in Fig. 12. The *R*-square (coefficient of determination) is used to represent the estimation accuracy of slant range history, which is defined as follows:

$$E_R = \frac{\sum_{n=1}^{N} \left(\hat{y}_n - \bar{y}_n\right)^2}{\sum_{n=1}^{N} \left(y_n - \bar{y}_n\right)^2} \tag{30}$$

where y_n is the truth value of the slant range history, $\hat{y}_n$ is the estimation result of y_n, and $\bar{y}_n$ is the mean value of y_n.

It is found that the *R*-square decreases as the SCR decreases. Before the SCR drops to -13 dB, the *R*-square decreases slowly. After the SCR is reduced to -13 dB, the *R*-square drops sharply.

Because the translational motion is the same to all the scatterers on a target, the influence of translation motion is not considered in analyzing the limitation on separating the adjacent scatterers. The slant range history of two adjacent scatterers, P_A and P_B, are written as follows:

$$R_A(\eta) = \sum_{k=1}^{K} A_{1,k} \sin\left(\omega_k \eta + \theta_{1,k}\right) \tag{31}$$

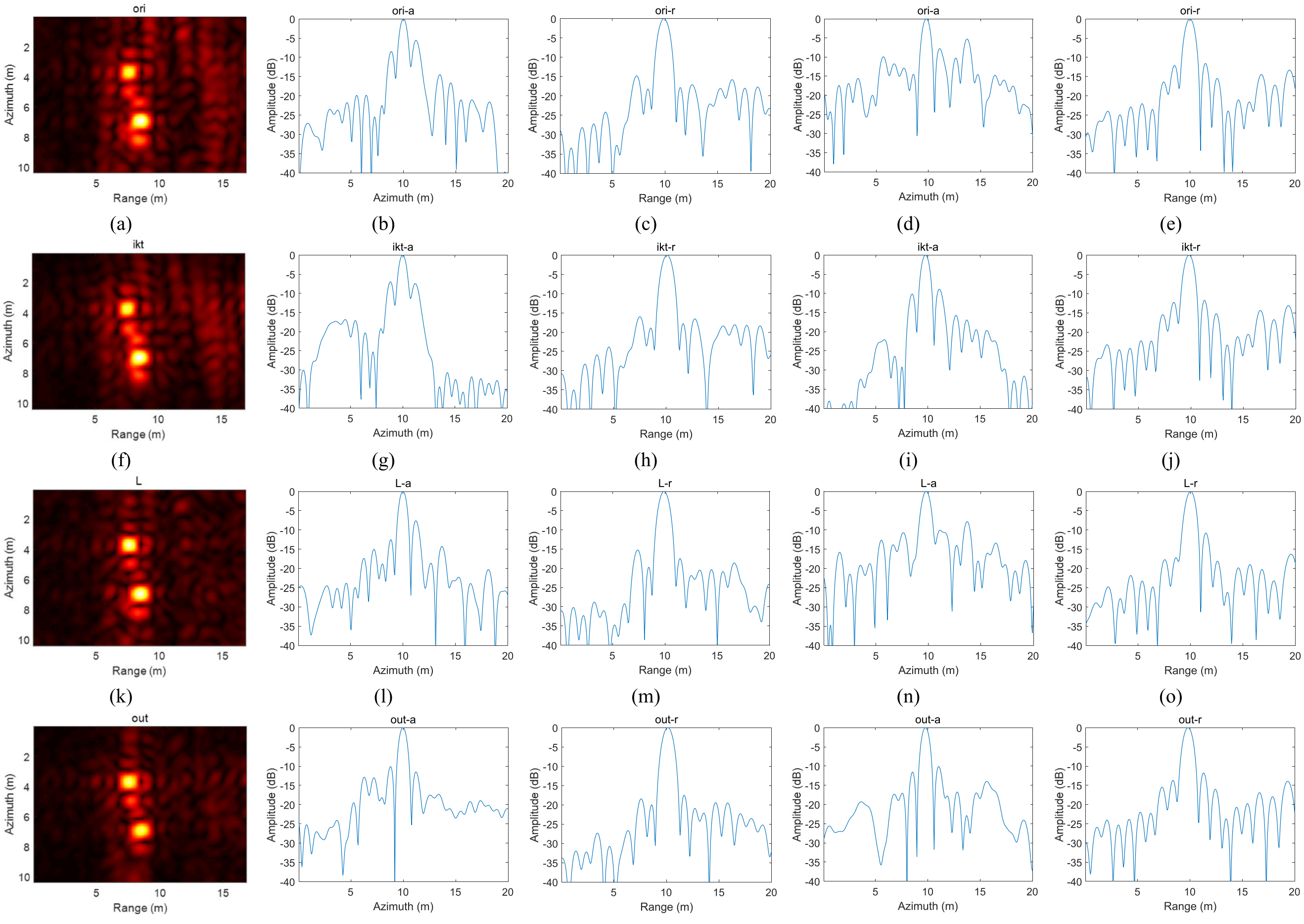

(a) (b) (c) (d) (e)

(f) (g) (h) (i) (j)

(k) (l) (m) (n) (o)

(p) (q) (r) (s) (t)

Fig. 11. Imaging results of real data achieved by the FT, KT and IKT, the L-statistics method, and the proposed method. (a), (f), (k), and (p) are the images achieved by these four methods, respectively. (b), (g), (l), and (q) are the azimuth profiles of S_1 achieved by these four methods, respectively. (c), (h), (m), and (r) are the range profiles of S_1 achieved by these four methods, respectively. (d), (i), (n), and (s) are the azimuth profiles of S_2 achieved by these four methods, respectively. (e), (j), (o), and (t) are the range profiles of S_2 achieved by these four methods, respectively.

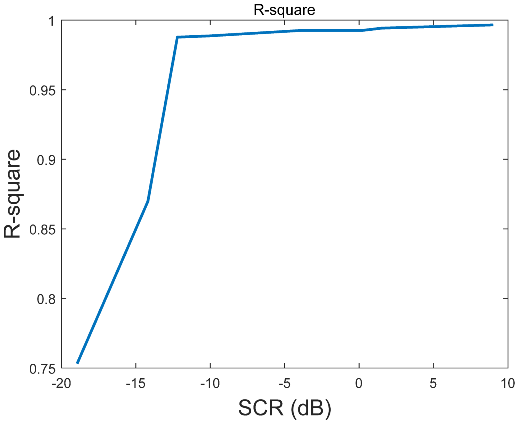

Fig. 12. Estimation accuracy in different clutter level.

and

$$R_B(\eta) = \sum_{k=1}^{K} A_{2,k}\sin(\omega_k\eta + \theta_{2,k}). \tag{32}$$

After the motion compensation of P_A, the residual slant range history of P_B is as follows:

$$\Delta R(\eta) = \sum_{k=1}^{K} A_{2,k}\sin(\omega_k\eta + \theta_{2,k}) - \sum_{k=1}^{K} A_{1,k}\sin(\omega_k\eta + \theta_{1,k}). \tag{33}$$

Then, each component of $\Delta R(\eta)$ is written as follows:

$$\Delta R_k(\eta) = A_{2,k}\sin(\omega_k\eta + \theta_{2,k}) - A_{1,k}\sin(\omega_k\eta + \theta_{1,k}). \tag{34}$$

After Keystone transform, $\Delta R_k(\eta)$ becomes

$$\begin{aligned}\Delta R_k(\eta) &= [A_{2,k}\sin(\omega_k\eta+\theta_{2,k}) - A_{2,k}\omega_k\eta\cos(\omega_k\eta+\theta_{2,k})]\\ &\quad - [A_{1,k}\sin(\omega_k\eta+\theta_{1,k}) - A_{1,k}\omega_k\eta\cos(\omega_k\eta+\theta_{1,k})]\\ &= A'_k\sin(\omega_k\eta + \varphi_{k,a}) - A'_k\omega\eta\sin(\omega_k\eta - \varphi_{k,b})\end{aligned} \tag{35}$$

where

$$A'_k = \sqrt{{A_{1,k}}^2 + {A_{2,k}}^2 - 2A_{1,k}A_{2,k}\cos\left(\theta_{1,k} - \theta_{2,k}\right)} \quad (36)$$

$$\varphi_{k,a} = \arctan\left[\frac{A_{2,k}\sin\left(\theta_{2,k}\right) - A_{1,k}\sin\left(\theta_{1,k}\right)}{A_{2,k}\cos\left(\theta_{2,k}\right) - A_{1,k}\cos\left(\theta_{1,k}\right)}\right] \quad (37)$$

and

$$\varphi_{k,b} = \pi/2 - \varphi_{k,a}. \quad (38)$$

$\Delta R_k(\eta)$ can be further expressed as follows:

$$\Delta R_k\left(\eta\right) = A'_k B'_k \sin\left(\omega\eta + {\varphi'}_k\right) \quad (39)$$

where

$$B'_k = \sqrt{1 + \omega^2\eta^2 - 2\omega\eta\cos\left(\varphi_{k,a} - \varphi_{k,b}\right)} \quad (40)$$

and

$$\varphi'_k = \arctan\left[\frac{\sin\left(\varphi_{k,a}\right) + \omega\eta\sin\left(\varphi_{k,b}\right)}{\cos\left(\varphi_{k,a}\right) - \omega\eta\cos\left(\varphi_{k,b}\right)}\right]. \quad (41)$$

When the amplitude of the residual motion of P_B is smaller than a range bin, i.e.

$$\left|\sum_{k=1}^{K} {A'}_k {B'}_k \sin\left(\omega\eta + {\varphi'}_k\right)\right| < p_r \quad (42)$$

the micro-motion removal in the range direction is ineffective. Specially, when the integration time of a subaperture is short that the slant range history can be expressed by a sine function, the limitation becomes

$$\left|{A'}_k {B'}_k \sin\left(\omega\eta + {\varphi'}_k\right)\right| \leq \left|{A'}_k {B'}_k\right| < p_r. \quad (43)$$

It is found that A'_k represents the relative position between P_A and P_B. B'_k represents the change of amplitude caused by Keystone transform.

A simulation experiment is implemented to help to analyze the limitation. The simulation is based on the parameters listed in Tables I and II. The results of simulation are shown in Figs. 13–16, where the distances between P_A and P_B are 5, 2, 1, and 0.5 m, respectively. All the experiments were implemented at an SCR of –5 dB. In order to show the change of RCM before and after the KT, the clutter is eliminated when showing the RCM results. But the processing is operated under the clutter.

From the results, it is found that the smallest distinguishable distance of two adjacent scatterers is 1 m in this simulation parameters.

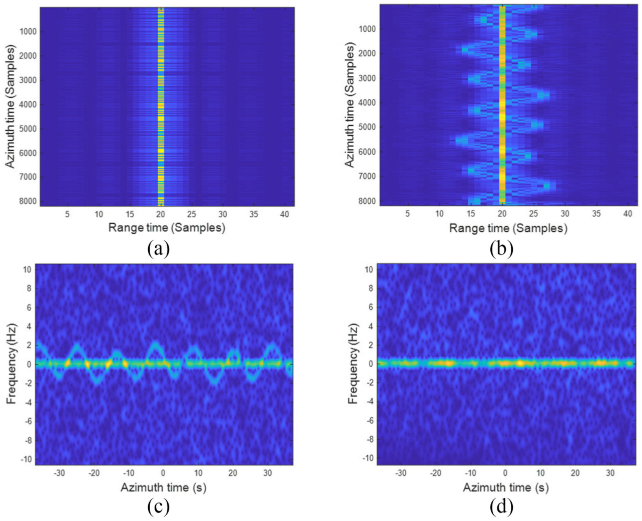

(a) (b)

(c) (d)

Fig. 13. Simulation results when the distance between the adjacent scatterers is 5 m. (a) and (c) are the RCM and TF results before the KT. (b) and (d) represent the RCM and TF results after the KT.

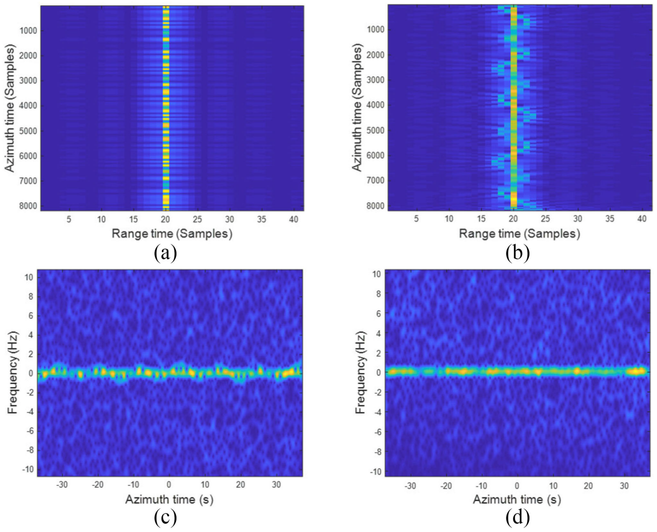

(a) (b)

(c) (d)

Fig. 14. Simulation results when the distance between the adjacent scatterers is 2 m. (a) and (c) are the RCM and TF results before the KT. (b) and (d) represent the RCM and TF results after the KT.

D. Computational Burden

The computational burden of high-dimensional parameter searching is mainly caused by GRFT.

Suppose that N_a and N_r are the total number of samples in the azimuth and range directions of the echo data, respectively, and the searching times of each parameter are assumed to be the same, denoted by N_0. The estimated high-dimensional parameters are listed as $[\hat{A}_{k,m}, \hat{\omega}_{k,m}, \hat{\theta}_{k,m}], k \in [1, K]$. The computational complexity of GRFT is $O[{N_0}^{3K} N_a N_r]$. The number of multiple sinusoidal functions K increases with the increasing integration time. Thus, high-dimensional parameter searching brings a heavy computational burden. Several strategies are adopted to reduce the computational burden while maintaining accuracy.

The subaperture segmentation method is used to reduce the order of polynomial or the number of multiple sinusoidal functions fitting in each subaperture. The number of subapertures is denoted as N_s, and the number of multiple sinusoidal functions becomes K_s. In addition, since the amplitude of micro-motion is limited, the RCM variation caused by the micro-motion is usually within several range bins. The number of range bins containing targets is denoted as N_{rs}.

The searching times of each parameter N_0 are reduced according to a priori knowledge. For example, the average amplitude and period of micro-motion are calculated based on the sea

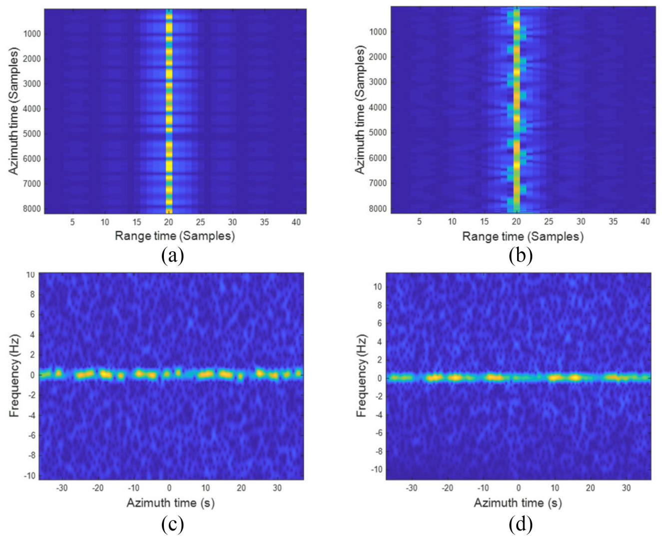

(a) (b)

(c) (d)

Fig. 15. Simulation results when the distance between the adjacent scatterers is 1 m. (a) and (c) are the RCM and TF results before the KT. (b) and (d) represent the RCM and TF results after the KT.

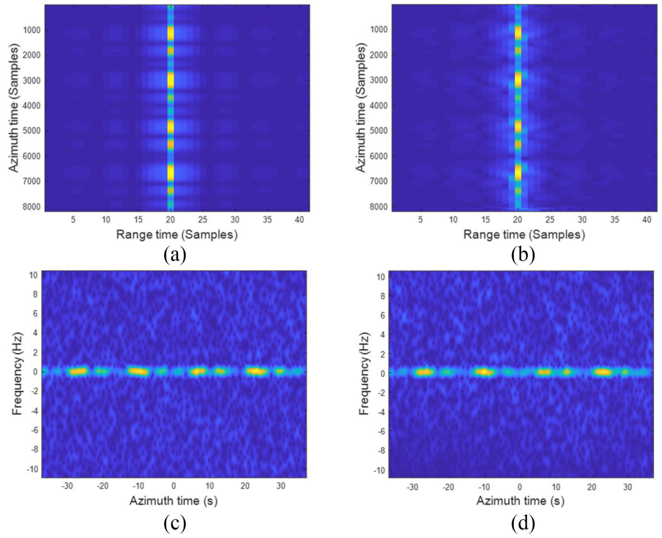

(a) (b)

(c) (d)

Fig. 16. Simulation results when the distance between the adjacent scatterers is 0.5 m. (a) and (c) are the RCM and TF results before the KT. (b) and (d) represent the RCM and TF results after the KT.

stage, wind speed, and type of ship. Moreover, the coarse TF relationship can be obtained by the method proposed in [27]. The initial values of parameter searching are calculated based on the coefficients of the TF relationship. Therefore, N_0 decreases.

The parameter searching interval varies from large to small. Coarse parameter searching with a large searching scope and large interval is performed first. Based on the coarse searching results, a fine parameter searching with a small searching scope and small interval is accomplished.

Then, the computational complexity becomes $O[{N_0}^{3K_s} N_a N_{rs}]$. Supposing that $N_a = 16\,384$, $N_r = 2048$, $N_0 = 40$, $N_s = 8$, $N_{rs} = 2$ and $K_s = 2$. The computational complexity is

$$C = 8 N_a N_{rs} {N_0}^{3k_s} = 1.0737 \times 10^{15}. \tag{44}$$

Even if the above strategies are adopted to reduce the computational complexity, a large computational complexity is still needed if the motion is sufficiently complex, and the integration time is long enough. However, with the improvement of the computational performance, these problems will become easier to solve.

VI. CONCLUSION

In this article, a three-step algorithm composed of GRFT-based motion compensation, partial micro-motion removal and intersections removal is proposed to accomplish signal separation in GEO SAR. The validation based on simulation and airborne experiments demonstrates that the proposed algorithm can achieve superior performance in signal separation. However, the computation of the GRFT operation prevents the real-time processing of the proposed algorithm, which will be concentrated on in the future.

APPENDIX A

Taking atmospheric turbulence into consideration, the GEO SAR system is affected by both ionospheric and tropospheric propagation [14].

First, the ionosphere is analyzed. Wang *et al.* [15] propose that the phase error induced by background ionosphere can be written as follows:

$$\Delta\phi = -\frac{2\pi \cdot 80.6 \cdot \mathrm{TEC}}{c \cdot f_c} \tag{45}$$

where TEC is the total electron content within the signal path, c is the light speed, and f_c is the signal frequency. The phase error induced by the ionosphere in C-band is smaller than L-band because of the higher frequency of C-band. The work [15] solves the problem induced by GEO SAR ionosphere. So, the ionosphere problem in the C-band is easier to solve.

Second, the troposphere is analyzed. The work in [14] indicates that the effect of the troposphere on imaging is time-varying and space-varying, which is the function of the position of the sensor along-track and the position of the target. Therefore, the influence of the troposphere is analyzed in both time variability and space variability. Fortunately, the ship covers a small area. The space variability induced by troposphere can be negligible. In the aspect of the time variability of troposphere, Tian *et al.* in [16] describe the phase error induced by troposphere as follows:

$$\begin{aligned}\Delta\phi_{trop}(\eta) &= \frac{4\pi}{\lambda} \cdot \Delta r(\eta) \\ &= \frac{4\pi}{\lambda} \cdot \left(\Delta r_0 + q_1\eta + q_2\eta^2 + q_3\eta^3 + \cdots\right)\end{aligned} \tag{46}$$

where $\Delta r(\eta)$ represents the range error induced by troposphere, Δr_0 is the constant part of $\Delta r(\eta)$, and $[q_1, q_2, q_3, \ldots]$ are the derivatives of each order of $\Delta r(\eta)$. According to the atmospheric refractivity profile data provided by the Chinese meteorological satellite FengYun-3 (FY-3) in [16], the second- and third-order derivative of tropospheric range error (q_2 and q_3) are -5.03×10^{-7} m/s^2 and 4.89×10^{-9} m/s^3, respectively [16].

The work in [12] indicates that it is sufficient to image the stationary target in GEO SAR by setting the order of the range history as 5. The order of the range history of moving target (with translational motion) in GEO SAR is set as 3 [28]. Therefore, the translation part of the range history without the influence of atmosphere is expressed as follows:

$$R'_{t,i}(\eta) = R_{0,t} + \sum_{n=1}^{5} r_{n,t}(\eta - \eta_i)^n \tag{47}$$

where $r_{2,t}$ and $r_{3,t}$ are 5.52×10^{-4} m/s^2 and -1.54×10^{-7} m/s^3, which are far larger than q_2 and q_3. Therefore, the range error induced by troposphere can be combined into a new range history with the translation part $R'_{t,i}(\eta)$, which is expressed as follows:

$$R_{t,i}(\eta) = R'_{t,i}(\eta) + \Delta r(\eta) = R_0 + \sum_{n=1}^{N_t} r_n(\eta - \eta_i)^n \tag{48}$$

where $R_0 = R_{0,t} + \Delta r_0$, $r_n = r_{n,t} + q_n, n \in [1, N_t]$, N_t depends on the larger one of the order of the translation part of range history and the order of the range error induced by troposphere. $R_{t,i}(\eta)$ represents the component influenced by ephemeris data, geographic information of the target zone, the translational motion of the targets and the troposphere. The coefficient r_n contains the influence of troposphere. The corresponding time-frequency relationship of the translation part is expressed as follows:

$$f_{t,i} = -\frac{2}{\lambda}\left[\sum_{n=1}^{N_t} r_n n(\eta - \eta_i)^{n-1}\right]. \tag{49}$$

When the submeters random variations of the troposphere enter in the instantaneous frequency model and affect the lower order coefficients, r_n changes and modulates the TF relationship. However, because the proposed algorithm has the ability to search coefficients adaptively, the motion compensation described in Section IV-A can estimate and compensate for the lower order coefficients even though it suffers from the influence of troposphere.

APPENDIX B

The original slant range history of (13) is as follows:

$$\begin{aligned} R_{grft}(\eta) &= R'_0 + {r_1}'\eta + {r_2}'\eta^2 + \Delta(\eta) \\ &\quad + \sum_{k=1}^{K'} {A'}_{k,i} \sin\left({\omega'}_{k,i}\eta + {\theta'}_{k,i}\right) \end{aligned} \tag{50}$$

where $R'_0 = R_0 - r_1\eta_i + r_2{\eta_i}^2$, ${r_1}' = r_1 - 2r_2\eta_i - \hat{r}_1$, and ${r_2}' = r_2 - \hat{r}_2$. Regarding different scatterers in a ship, ${r_1}'$ is different because of the influence of the $\eta_i$term. However, ${r_2}'$is compensated if $\hat{r}_2$ is exact. $\Delta(\eta)$ represents high-order residual terms corresponding to r_3, r_4, and r_5.

The influence of r_3, r_4, and r_5 on slant range and frequency is analyzed here. A target of 500 m × 500 m is simulated, as shown in Fig. 17(a). The distance between adjacent points is 50 m. And the parameters of GEO SAR are the same as Table I.

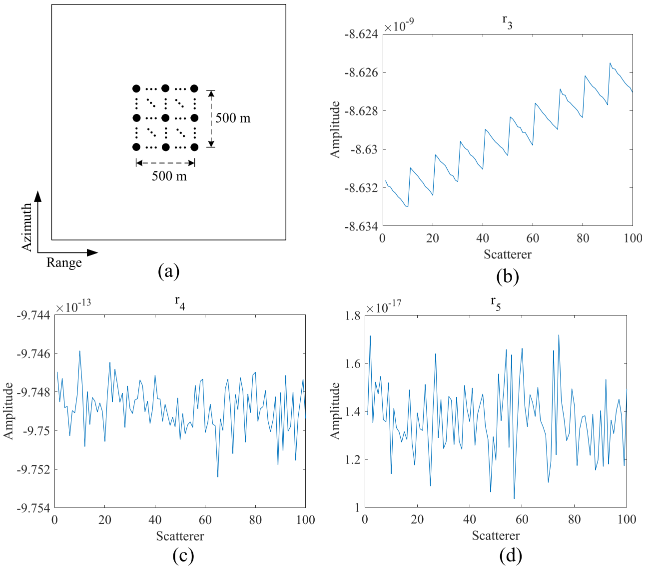

Fig. 17. Analysis of coefficients of slant range. (a) Simulation scene containing a target of 500 m × 500 m. (b)–(d) represent the varying of r_3–r_5 with positions, respectively.

The amplitude of r_3–r_5 varying with positions in the target is depicted in Fig. 17(b)–(d), respectively. Considering the long integration time, the maximum slant range terms in (3) corresponding to r_3, r_4, and r_5, i.e., $r_3\eta^3$, $r_4\eta^4$, and $r_5\eta^5$, are 3.70×10^{-4}, 1.46×10^{-6}, and 8.86×10^{-10} m, respectively, the corresponding maximum frequency change are 0.0013, 6.69×10^{-6}, and 5.06×10^{-9} Hz, respectively.

Compared with the range resolution and frequency resolution, $\Delta(\eta)$ can be ignored in the following analysis. Therefore, (50) can be simplified as follows:

$$R_{grft}(\eta) = R'_0 + {r_1}'\eta + \sum_{k=1}^{K'} {A'}_{k,i} \sin\left({\omega'}_{k,i}\eta + {\theta'}_{k,i}\right). \tag{51}$$

APPENDIX C

The range Fourier transform of (12) can be expressed as follows:

$$S_{grft}(f_\tau, \eta) = {w_a}'(\eta)\, \mathcal{F}_\tau\left[p_r(\tau)\right] \exp\left[j\varphi(f_\tau, \eta)\right] \tag{52}$$

where

$${w_a}'(\eta) = A_0 w_a(\eta - \eta_i) \tag{53}$$

$$\begin{aligned} \varphi(f_\tau, \eta) &= -\frac{4\pi}{c}(f_c + f_\tau) \\ &\qquad \left[{R'}_0 + {r_1}'\eta + \sum_{k=1}^{K'} {A'}_{k,i} \sin\left({\omega'}_{k,i}\eta + {\theta'}_{k,i}\right)\right]. \end{aligned} \tag{54}$$

Substituting (16) into (54), $\varphi(f_\tau, t_a)$ can be written as follows:

$$\varphi\left(f_\tau, t_a\right)=-\frac{4\pi}{c}\begin{bmatrix}\left(f_c+f_\tau\right) R'_0+{r_1}' f_c t_a \\ +\left(f_c+f_\tau\right) \sum\limits_{k=1}^{K'} A'_{k,i} \\ \sin\left(\omega'_{k,i} \frac{f_c}{f_c+f_\tau} t_a+\theta'_{k,i}\right)\end{bmatrix}. \tag{55}$$

Because RCM is only related to terms with f_τ, $\varphi(f_\tau, t_a)$ is divided into two parts. One part contains terms without f_τ, named as $\varphi_1(t_a)$, and the other part is composed of the terms related to f_τ, named, $\varphi_2(f_\tau, t_a)$

$$\varphi\left(f_\tau, t_a\right)=\varphi_1\left(t_a\right)+\varphi_2\left(f_\tau, t_a\right) \tag{56}$$

where

$$\varphi_1\left(t_a\right)=-\frac{4\pi}{\lambda}\left[{R_0}'+{r_1}' t_a+\sum_{k=1}^{K'} A'_{k,i} \sin\left(\omega'_{k,i} t_a+\theta'_{k,i}\right)\right]. \tag{57}$$

$\varphi_2(f_\tau, t_a)$ can be formulated by Taylor expansion as follows:

$$\varphi_2\left(f_\tau, t_a\right)=-\frac{4\pi}{c}\left[R_{KT}\left(t_a\right) f_\tau+D_2 {f_\tau}^2+D_3 {f_\tau}^3+\Delta\left(f_\tau\right)\right] \tag{58}$$

where $R_{KT}(t_a)$, D_2, and D_3 are coefficients corresponding to the first-, the second-. and the third-order terms, which can be written as follows in detail:

$$\begin{cases} R_{\mathrm{KT}}\left(t_a\right)=R'_0+\sum_{k=1}^{K'}\begin{bmatrix}A'_{k,i} \sin\left(\omega'_{k,i} t_a+\theta'_{k,i}\right) \\ -A'_{k,i} \omega'_{k,i} t_a \cos\left(\omega'_{k,i} t_a+\theta'_{k,i}\right)\end{bmatrix} \\ D_2=-\sum_{k=1}^{K'} \frac{A'_{k,i} {\omega'_{k,i}}^2 {t_a}^2}{2 f_c} \sin\left(\omega'_{k,i} t_a+\theta'_{k,i}\right) \\ D_3=\sum_{k=1}^{K'}\begin{bmatrix}\frac{A'_{k,i} {\omega'_{k,i}}^2 {t_a}^2}{2 {f_c}^2} \sin\left(\omega'_{k,i} t_a+\theta'_{k,i}\right) \\ +\frac{A'_{k,i} {\omega'_{k,i}}^3 {t_a}^3}{6 {f_c}^2} \cos\left(\omega'_{k,i} t_a+\theta'_{k,i}\right)\end{bmatrix}. \end{cases} \tag{59}$$

$\Delta(f_\tau)$ represents high-order terms of f_τ. Usually, the carrier frequency f_c is far larger than half of the integration time, which is the maximum value of t_a. Therefore, compared with $R_{\mathrm{KT}}(t_a)$ in (58), D_2, D_3, and the coefficients of high-order terms are smaller due to the influence of f_c.

APPENDIX D

Applying range Fourier transform to (23), the result is

$$\begin{aligned} S_w\left(f_\tau, t_a\right)&={w_a}'\left(t_a\right) \mathcal{F}_\tau\left[{w_r}'\left(\tau, t_a\right)\right] \\ &\times \exp\left\{-j \tfrac{4\pi}{\lambda}\left[{R_0}'+{r_1}' t_a+\sum_{k=1}^{K'} A'_{k,i} \sin\left(\omega'_{k,i} t_a+\theta'_{k,i}\right)\right]\right\}. \end{aligned} \tag{60}$$

Substituting (24) into (60), the result is as follows:

$$\begin{aligned} S_{\mathrm{IKT}}\left(f_\tau, \eta\right)&={w_a}'(\eta) \cdot \mathcal{F}_\tau\left[w_{s,i}(\tau, \eta) \cdot p_r(\tau)\right] \\ &\times \exp\left\{-j \frac{4\pi}{c}\begin{bmatrix}R_{\mathrm{KT}}\left[\eta\left(f_c+f_\tau\right)/f_c\right] f_\tau \\ +D_2 {f_\tau}^2+D_3 {f_\tau}^3+\Delta\left(f_\tau\right)\end{bmatrix}\right\} \\ &\times \exp\left\{-j \frac{4\pi}{\lambda}\begin{bmatrix}{R_0}'+{r_1}' \frac{f_c+f_\tau}{f_c} \eta \\ +\sum_{k=1}^{K'} A'_{k,i} \sin\left(\omega'_{k,i} \frac{f_c+f_\tau}{f_c} \eta+\theta'_{k,i}\right)\end{bmatrix}\right\} \end{aligned} \tag{61}$$

TABLE VIII
PARAMETER ESTIMATION RESULTS OF T_1

Coefficient	Subaperture 1		Subaperture 2		Subaperture 3	
$\hat{A}_{k,m}$	2.8714	0.5043	0.8703	0.4167	1.6930	0.3201
$\hat{\omega}_{k,m}$	0.0020	0.4857	0.1250	0.5459	0.0292	0.5654
$\hat{\theta}_{k,m}$	3.0001	-0.0360	1.3752	-1.0084	2.7202	-2.1249
Coefficient	Subaperture 4		Subaperture 5		Subaperture 6	
$\hat{A}_{k,m}$	0.6495	0.4427	1.0538	0.3191	1.1733	0.4287
$\hat{\omega}_{k,m}$	0.0900	0.5283	0.0660	0.5771	0.0299	0.5143
$\hat{\theta}_{k,m}$	0.8926	-2.9932	0.8679	-4.1378	2.1363	1.1028
Coefficient	Subaperture 7		Subaperture 8			
$\hat{A}_{k,m}$	2.0375	0.3391	0.6987	0.4551		
$\hat{\omega}_{k,m}$	0.0163	0.5735	0.0871	0.5239		
$\hat{\theta}_{k,m}$	2.7817	-0.1176	1.4053	-1.0999		

TABLE IX
PARAMETER ESTIMATION RESULTS OF T_2

Coefficient	Subaperture 1		Subaperture 2		Subaperture 3	
$\hat{A}_{k,m}$	1.0357	0.5357	0.9940	0.4940	0.3514	1.5829
$\hat{\omega}_{k,m}$	0.0391	0.5560	0.0833	0.5756	0.6000	0.1000
$\hat{\theta}_{k,m}$	-0.0712	0.0038	1.0414	-0.9690	-2.1520	-2.1020
Coefficient	Subaperture 4		Subaperture 5		Subaperture 6	
$\hat{A}_{k,m}$	0.4016	0.6516	0.8037	0.4217	1.1895	0.5131
$\hat{\omega}_{k,m}$	0.1500	0.5144	0.1167	0.5878	0.1000	0.5389
$\hat{\theta}_{k,m}$	0.0492	-3.0621	0.9084	-4.1248	1.7244	1.0823
Coefficient	Subaperture 7		Subaperture 8			
$\hat{A}_{k,m}$	0.4937	0.4937	0.3383	0.5883		
$\hat{\omega}_{k,m}$	0.1000	0.5633	0.0667	0.5389		
$\hat{\theta}_{k,m}$	3.1288	-0.1120	0.6301	-1.0853		

where $w_{s,i}(\tau, \eta)$ is an equivalent window function corresponding to the scope of the red RCM curve (designed for the ith scatterer) among range bin C in Fig. 4(e). It is worth noting that the generation of $w_{s,i}(\tau, \eta)$ is caused by the elimination of part energy of the red scatterer beyond range bin C after KT.

After the inverse Fourier transform in the range direction, (61) becomes

$$\begin{aligned} S_{\mathrm{IKT}}(\tau, \eta)&={w_a}'(\eta)\, w_{s,i}(\tau, \eta)\, p_r\left[\tau-\tfrac{2 R_{\mathrm{IKT}}(\eta)}{c}\right] \\ &\times \exp\left\{-j \tfrac{4\pi}{\lambda} R_{\mathrm{IKT}}(\eta)\right\} \end{aligned} \tag{62}$$

where

$$R_{\mathrm{IKT}}(\eta)=R'_0+{r_1}' \eta+\sum_{k=1}^{K'} A'_{k,i} \sin\left(\omega'_{k,i} \eta+\theta'_{k,i}\right). \tag{63}$$

TABLE X
PARAMETER ESTIMATION RESULTS OF T_3

Coefficient	Subaperture 1		Subaperture 2		Subaperture 3	
$\hat{A}_{k,m}$	0.6659	7.1113	1.2138	0.6436	2.1681	0.5768
$\hat{\omega}_{k,m}$	0.5570	0.0087	0.0894	0.5681	0.0415	0.5606
$\hat{\theta}_{k,m}$	-0.0214	0.0585	1.1093	-0.9713	2.7082	-2.1189
Coefficient	Subaperture 4		Subaperture 5		Subaperture 6	
$\hat{A}_{k,m}$	1.1135	0.9403	1.4096	0.5556	1.5244	0.6372
$\hat{\omega}_{k,m}$	0.1145	0.4915	0.0855	0.5860	0.1060	0.5478
$\hat{\theta}_{k,m}$	0.5346	-3.0284	0.8660	-4.1344	1.6974	1.0763
Coefficient	Subaperture 7		Subaperture 8			
$\hat{A}_{k,m}$	6.5534	0.6297	1.2324	0.7520		
$\hat{\omega}_{k,m}$	0.0099	0.5647	0.0242	0.5349		
$\hat{\theta}_{k,m}$	3.0054	-0.1131	0.6757	-1.0837		

TABLE XI
PARAMETER ESTIMATION RESULTS OF TRANSLATION IN REAL DATA

Parameter Name	Estimated Value
$\hat{r}_0$	-284.2
$\hat{r}_1$	-1.951
$\hat{r}_2$	0.1002

APPENDIX E

According to the analysis in Appendix A, r_3, r_4, and r_5 has little influence on the slant range based on the parameters listed in Table I. Therefore, r_3, r_4, and r_5 are calculated according to GEO SAR observation geometry directly, denoted as $\hat{r}_3$, $\hat{r}_4$, and $\hat{r}_5$, respectively. r_1 and r_2 are estimated by GRFT, which are denoted as $\hat{r}_1$ and $\hat{r}_2$, respectively.

Due to the long integration time of simulation data, the data are divided into eight subapertures. In each subaperture, two sinusoidal functions are used to represent the slant range caused by micro-motion. The micro-motion part is written as follows:

$$\hat{R}_m(\eta) = \sum_{k=1}^{2} \hat{A}_{k,m} \sin\left(\hat{\omega}_{k,m}\eta + \hat{\theta}_{k,m}\right) \tag{64}$$

where

$$\eta \in \left[-\frac{T}{2} + \frac{(n_s - 1)T}{N_s}, -\frac{T}{2} + \frac{n_s T}{N_s}\right]. \tag{65}$$

N_s is the total number of subapertures ($N_s = 8$ in this simulation) and $n_s = [1, 2, \ldots, N_s]$.

The estimation results of translational motion are listed in Table VII. The parameter estimation estimated results of T_1, T_2, and T_3 are listed in Tables VIII–X, respectively.

The integration time of real data is approximately 18 s. From the time-frequency relationship of Fig. 10, we know that it contains approximately two periods of micro-motion during the integration time. Thus, three sinusoidal functions are used to establish the model of the micro-motion part. The estimation results of translational motion and micro-motion are listed in Tables XI and XII, respectively.

TABLE XII
PARAMETER ESTIMATION RESULTS OF MICRO-MOTION IN REAL DATA

Scatterer	Parameter Name	Estimated Value		
1	$\hat{A}_{k,m}$	3.417	0.491	3.468
	$\hat{\omega}_{k,m}$	0.392	0.908	0.384
	$\hat{\theta}_{k,m}$	1.968	1.095	-1.179
2	$\hat{A}_{k,m}$	1.571	0.223	1.576
	$\hat{\omega}_{k,m}$	0.390	0.915	0.382
	$\hat{\theta}_{k,m}$	2.090	1.076	-1.061

REFERENCES

[1] K. Tomiyasu and J. L. Pacelli, “Synthetic aperture radar imaging from an inclined geosynchronous orbit,” *IEEE Trans. Geosci. Remote Sens.*, vol. GE-21, no. 3, pp. 324–329, Jul. 1983.

[2] W. Xiong, Y. Zhang, X. Dong, C. Cui, Z. Liu, and M. Xiong, “A novel ship imaging method with multiple sinusoidal functions to match rotation effects in geosynchronous SAR,” *Remote Sens.*, vol. 12, 2020, Art. no. 2249.

[3] X. Li, B. Deng, Y. Qin, H. Wang, and Y. Li, “The influence of target micromotion on SAR and GMTI,” *IEEE Trans. Geosci. Remote Sens.*, vol. 49, no. 7, pp. 2738–2751, Jul. 2011.

[4] V. C. Chen, F. Li, S. S. Ho, and H. Wechsler, “Micro-Doppler effect in radar: Phenomenon, model, and simulation study,” *IEEE Trans. Aerosp. Electron. Syst.*, vol. 42, no. 1, pp. 2–21, Jan. 2006.

[5] L. Stankovic, M. Dakovic, T. Thayaparan, and V. Popovic-Bugarin, “Inverse radon transform-based micro-doppler analysis from a reduced set of observations,” *IEEE Trans. Aerosp. Electron. Syst.*, vol. 51, no. 2, pp. 1155–1169, Apr. 2015.

[6] Q. Zhang, T. S. Yeo, H. S. Tan, and Y. Luo, “Imaging of a moving target with rotating parts based on the Hough transform,” *IEEE Trans. Geosci. Remote Sens.*, vol. 46, no. 1, pp. 291–299, Jan. 2008.

[7] T. Thayaparan, S. Abrol, E. Riseborough, L. Stankovic, D. Lamothe, and G. Duff, “Analysis of radar micro-Doppler signatures from experimental helicopter and human data,” *IET Radar, Sonar Navig.*, vol. 1, no. 4, pp. 289–299, Aug. 2007.

[8] R. Zhang, G. Li, and Y. D. Zhang, “Micro-Doppler interference removal via histogram analysis in time-frequency domain,” *IEEE Trans. Aerosp. Electron. Syst.*, vol. 52, no. 2, pp. 755–768, Apr. 2016.

[9] L. Stankovic, T. Thayaparan, M. Dakovic, and V. Popovic-Bugarin, “Micro-Doppler removal in the radar imaging analysis,” *IEEE Trans. Aerosp. Electron. Syst.*, vol. 49, no. 2, pp. 1234–1250, Apr. 2013.

[10] X. Chen, J. Guan, Z. Bao, and Y. He, “Detection and extraction of target with micromotion in spiky sea clutter via short-time fractional fourier transform,” *IEEE Trans. Geosci. Remote Sens.*, vol. 52, no. 2, pp. 1002–1018, Feb. 2014.

[11] D. Pastina, A. Montanari, and A. Aprile, “Motion estimation and optimum time selection for ship ISAR imaging,” in *Proc. IEEE Radar Conf.*, 2003, pp. 7–14, doi: 10.1109/NRC.2003.1203371.

[12] J. Geng, Z. Yu, C. Li, and W. Liu, “Squint mode GEO SAR imaging using bulk range walk correction on received signals,” *Remote Sens.*, vol. 11, 2019, Art. no. 17.

[13] Z. Yu, P. Lin, P. Xiao, L. Kang, and C. Li, “Correcting spatial variance of RCM for GEO SAR imaging based on time-frequency scaling,” *Sensors*, vol. 16, no. 7, Jul. 2016, Art. no. 1091.

[14] A. Monti Guarnieri, A. Leanza, A. Recchia, S. Tebaldini, and G. Venuti, “Atmospheric phase screen in GEO-SAR: Estimation and compensation,” *IEEE Trans. Geosci. Remote Sens.*, vol. 56, no. 3, pp. 1668–1679, Mar. 2018.

[15] R. Wang *et al.*, “Joint amplitude-phase compensation for ionospheric scintillation in GEO SAR imaging,” *IEEE Trans. Geosci. Remote Sens.*, vol. 55, no. 6, pp. 3454–3465, Jun. 2017.

[16] Y. Tian, C. Hu, X. Dong, and T. Zeng, "Analysis of effects of time variant troposphere on Geosynchronous SAR imaging," in *Proc. IEEE Int. Geosci. Remote Sens. Symp.*, 2016, pp. 5051–5054.

[17] P. Huang, G. Liao, Z. Yang, X. G. Xia, J. T. Ma, and J. Ma, "Long-time coherent integration for weak maneuvering target detection and high-order motion parameter estimation based on keystone transform," *IEEE Trans. Signal Process.*, vol. 64, no. 15, pp. 4013–4026, Aug. 2016.

[18] J. Xu, X. Xia, S. Peng, J. Yu, Y. Peng, and L. Qian, "Radar maneuvering target motion estimation based on generalized radon-Fourier transform," *IEEE Trans. Signal Process.*, vol. 60, no. 12, pp. 6190–6201, Dec. 2012.

[19] Y. Zhang, W. Xiong, X. Dong, C. Hu, and Y. Sun, "GRFT-Based moving ship target detection and imaging in geosynchronous SAR," *Remote Sens.*, vol. 10, pp. 2018, Art. no. 2002.

[20] M. Jiang, W. Hu, C. Ding, and G. Liu, "The effects of orbital perturbation on geosynchronous synthetic aperture radar imaging," *IEEE Geosci. Remote Sens. Lett.*, vol. 12, no. 5, pp. 1106–1110, May 2015.

[21] S. Yuan, C. Li, Z. Yu, J. Geng, and J. Yu, "Maximum Nesigma0 based on the new steering strategy for Geo Sar," in *Proc. IEEE Int. Geosci. Remote Sens. Symp.*, 2019, pp. 8633–8636.

[22] Z. Ding, W. Yin, T. Zeng, and T. Long, "Radar parameter design for Geosynchronous SAR in squint mode and elliptical orbit," *IEEE J. Sel. Topics Appl. Earth Observ. Remote Sens.*, vol. 9, no. 6, pp. 2720–2732, Jun. 2016.

[23] S. Hobbs, C. Mitchell, B. Forte, R. Holley, B. Snapir, and P. Whittaker, "System design for Geosynchronous synthetic aperture radar missions," *IEEE Trans. Geosci. Remote Sens.*, vol. 52, no. 12, pp. 7750–7763, Dec. 2014.

[24] C. Hu, T. Long, Z. Liu, T. Zeng, and Y. Tian, "An improved frequency domain focusing method in geosynchronous SAR," *IEEE Trans. Geosci. Remote Sens.*, vol. 52, no. 9, pp. 5514–5528, Sep. 2014.

[25] C. Hu, T. Long, T. Zeng, F. Liu, and Z. Liu, "The accurate focusing and resolution analysis method in geosynchronous SAR," *IEEE Trans. Geosci. Remote Sens.*, vol. 49, no. 10, pp. 3548–3563, Oct. 2011.

[26] T. Zhang *et al.*, "The first helicopter platform-based equivalent GEO SAR experiment with long integration time," *IEEE Trans. Geosci. Remote Sens.*, vol. 58, no. 12, pp. 8518–8530, Dec. 2020.

[27] J. Yu, Z. Yu, and C. Li, "Parameters estimation of high speed maneuvering target with micro motion in geosar," in *Proc. IEEE Int. Geosci. Remote Sens. Symp.*, 2019, pp. 497–500.

[28] M. Melzi, C. Hu, X. Dong, Y. Li, and C. Cui, "Velocity estimation of multiple moving targets in single-channel geosynchronous SAR," *IEEE Trans. Geosci. Remote Sens.,* vol. 58, no. 8, pp. 5861–5879, Aug. 2020.

Jindong Yu (Student Member, IEEE) was born in Tianjin, China, in 1992. He received the B.S. degree in electronics engineering in 2015 from Beihang University, Beijing, China, where he is currently working toward the Ph.D. degree in signal and information processing.

His research interests include system analysis and imaging processing for synthetic aperture radar moving target.

Ze Yu (Member, IEEE) was born in Xi'an, China, in 1979. He received the B.S. degree in electronics engineering and the Ph.D. degree in communication and information system from Beihang University, Beijing, China, in 2002 and 2007, respectively.

Since 2009, he has been with the School of Electronics and Information Engineering, Beihang University. He is currently involved in the system design and imaging processing for high-resolution and wide-swath synthetic aperture radar.

Yukun Guo was born in Beijing, China, in 1990. He received the B.S. degree in electronics engineering in 2013 from Beihang University, Beijing, where he is currently working toward the Ph.D. degree in signal and information processing.

His research interests include system performance analysis and signal processing for multistatic synthetic aperture radar.

Chunsheng Li received the Ph.D. degree in signal and information processing from Beihang University, Beijing, China, in 1998.

Since 2005, he has been a Professor with the School of Electronics and Information Engineering, Beihang University. He has authored more than 100 journal and conference papers and four books. His research interests include analysis and simulation of spaceborne synthetic aperture radar, high-resolution image formation, and multimodal remote sensing data fusion.